Electrochimica Acta 298 (2019) 254–264

Contents lists available at ScienceDirect

Electrochimica Acta

journal homepage: www.elsevier.com/locate/electacta

Tuning capacitance of graphene films via a robust routine of adjusting their hierarchical structures

Fei Dang [a], Pengfei Yang [a], Wei Zhao [b], Jefferson Zhe Liu [c], Huaping Wu [d], Aiping Liu [e, **], Yilun Liu [a, *]

[a] State Key Laboratory for Strength and Vibration of Mechanical Structures, School of Aerospace Engineering, Xi'an Jiaotong University, Xi'an 710049, China
[b] School of Chemical Engineering, Northwest University, Xi'an 710069, China
[c] Department of Mechanical Engineering, The University of Melbourne, Melbourne, VIC 3010, Australia
[d] Key Laboratory of E&M (Zhejiang University of Technology), Ministry of Education & Zhejiang Province, Hangzhou 310014, China
[e] Nanometer Measurement Laboratory, Center for Optoelectronics Materials and Devices, Zhejiang Sci-Tech University, Hangzhou 310018, China

ARTICLE INFO

Article history:
Received 5 October 2018
Received in revised form
13 November 2018
Accepted 13 December 2018
Available online 14 December 2018

Keywords:
Graphene film
Hierarchical structures
Enhanced electrical conductivity
Tunable capacitance
Supercapacitor

ABSTRACT

In this work, the nitrogen doped graphene films with hierarchical network structures have been successfully fabricated via a robust routine of adjusting the content of large- and small-sized reduced graphene oxide (RGO) sheets in the graphene films, where the large-sized RGO sheets act as the backbone to form the well-connected network structures and small-sized RGO sheets act as the interlayer and interpore linkers to connect the large-sized RGO sheets and large pores. A maximum capacitance of 429.7 F g^{-1} is obtained for the optimized RGO electrode with small-sized RGO content of 40 wt%, which is 61.9% improvement compared to the RGO electrodes with pure large-sized RGO sheets. While, the specific surface area and electrical conductivity of the optimized RGO electrode are 36.1% and 26.2% improvement compared to the pure large-sized electrode. Therefore, we attribute the improved capacitance primarily comes from the increasing of specific surface area due to the formation of fine hierarchical structures and the better connection of the network structures (the increasing of electrical conductivity) for the optimized RGO electrode. Besides, the optimized RGO electrode exhibits good cycle, rate performance, power and energy density compared to the previous carbon based supercapacitor. Herein, we can precisely control the specific surface area and electrical conductivity of RGO electrode by simply adjusting the content of large- and small-sized RGO, which may shed useful insight for the design of high performance supercapacitors and Li-ion batteries.

1. Introduction

Supercapacitors, as a kind of electrochemical energy storage system, have drawn substantial attentions due to their advantages over conventional batteries, such as high power density and long cycle life [1–3]. They can provide several times more power density than that of the current state-of-the-art lithium-ion batteries due to their fast surface-charge-storage process, which have been proposed as one of the ideal energy storage candidates for fast energy supply. Besides, supercapacitors can be used in combination with batteries to compensate the deficiency of power density for electrochemical batteries. In general, electrochemical capacitors have two categories, i.e. electrostatic double-layer capacitor (EDLC) due to the charging and discharging of the electrical double layer at the interface between the electrode and electrolyte [4], and electrochemical pseudocapacitor due to the reversible redox reactions of the electrode materials [5].

With the continuous demanding of high performance energy storage system, much research has been devoted to developing high performance electrode materials that is one of the key factors to determine the supercapacitor performance [6–8]. Chemically modified graphene prepared by simple chemical treatment of graphite [9,10], holds great promise for excellent electrode materials because of its superior properties, such as low-cost, easy mass production, good electrical conductivity, exceptional surface area, and long-term electrochemical stability [11–13]. However, the

* Corresponding author.
** Corresponding author.
E-mail addresses: liuaiping1979@gmail.com (A. Liu), yilunliu@mail.xjtu.edu.cn (Y. Liu).

https://doi.org/10.1016/j.electacta.2018.12.071
0013-4686/

specific capacitance of graphene based EDLC reported before is much smaller than the theoretical upper limit capacitance of graphene sheet, namely 550 Fg^{-1} [14–16]. Thus, the challenge is to develop graphene related materials with well-connected network structures and high specific surface area to fully explore the capability of the capacitance of graphene. Besides, the chemically modified graphene has rich catalogues of functionalized groups and the incorporation of heteroatoms into graphene is a promising strategy to tune its electrical performance [17,18]. Liu et al. distributed oxygen clusters in graphene framework with "paddy land" structures which exhibit good capacitance and rate performance [19]. Besides, a number of experiments have shown that the incorporation of nitrogen (N) [20] and sulfur (S) [21] to graphene can further tailor the chemical properties of graphene so as to enhance the electrochemical performances through the reversible redox reactions.

Graphene film, or graphene paper, is superior to many other paper-like materials in layered structure. Various methods have been proposed to fabricate graphene films, such as interfacial self-assembly [22], spry-coating [23], blade-coating [24], layer-by-layer assembly [25], evaporation-induced self-assembly [26] and filtration [27,28]. However, owing to the interlayer π-π interaction, the two dimensional graphene sheets is easy to stack into densely packed structures during the fabrication process, which doesn't fully utilize the large specific surface area of graphene sheet and leads to the reduction of capacitance and rate performance of graphene film electrodes. Yang et al. pointed out that the presence of nonvolatile electrolyte can prevent the dense π-π stacking structures [29]. Xiong et al. developed a feasible method to prepare flexible large-area hierarchical porous graphene films for high-performance supercapacitor electrodes by the blade-casting technique [30,31]. The hierarchical porous graphene films with interlinked and oriented structure exhibit high strength and excellent toughness [32]. Recently, Shao et al. reported that the graphene films fabricated by filtration and freeze-casting exhibit three dimensional porous network structures. The porous network structures can act as ion-buffering reservoirs and ion-transport channels for electrochemical kinetic possesses [33]. The previous studies mainly focused on preparing graphene films with relatively uniform size of graphene sheets, and the obtained capacitance was still smaller than the theoretical ideal capacitance of graphene sheet. Few studies found the integration of large- and small-sized graphene sheets can form hierarchical structures of graphene films or fibers to enhance their mechanical, thermal and electrical properties [34]. Besides, the well-connected network structures of holely-graphene/niobia composite is found to exhibit fast ion transport to achieve ultrahigh-rate energy storage [35]. But, in these works the hierarchical structures of graphene electrode weren't well controlled and the relation of structure-property for graphene related electrode materials has not been comprehensively explored. Therefore, it is very important to develop a simple method to synthesize graphene electrodes with hierarchical structures to explore the relation of process-structure-property of graphene electrode materials.

In this work, we present a simple method to fabricate the nitrogen doped graphene films with well-connected hierarchical structures through properly adjusting the content of large- and small-sized graphene sheets in the films. The reduced graphene oxide (RGO) sheets with nitrogen doping are prepared by chemical reduction of graphene oxide (GO) with ethylenediamine (EDA) and assembled to RGO films by combining the vacuum filtration and freeze-drying methods. The optimized RGO films with proper content of large- and small-sized RGO sheets have fine and well-connected hierarchical structures, thus exhibiting higher specific surface area, electrical conductivity, and more excellent capacitive performances. Furthermore, the hierarchical RGO films reported herein could also have promising potential for extensive applications, such as batteries, sensors and gas absorption.

2. Experimental

2.1. Synthesis of GO

Here, graphene oxide was synthesized by the oxidation of natural graphite powder according to the modified Hummers' method [36]. Typically, 1 g graphite powder and 0.5 g $NaNO_3$ were added to the 25 mL concentrated H_2SO_4 in a round-bottom flask, and were stirred for 2 h in an ice-bath. Then, 3 g $KMnO_4$ was slowly added to the mixture for further reaction of 2 h. Next, the round-bottom flask was put to an oil-bath at 35 ± 3 °C and stirred vigorously for 2 h. After dilution with 45 mL deionized (DI) water, the mixture was reacted for further 30 min at 95 °C. After diluting with 28 mL DI water and treating with 3.5 mL H_2O_2, it turned to bright yellow color. Finally, the mixture was filtered and washed with HCl aqueous solution and DI water until neutral. Large-sized graphene oxide (LGGO) and small-sized graphene oxide (SMGO) were prepared by oxidizing 325 mesh and 8000 mesh graphite, which showed much larger size of LGGO (Fig. S1a) than that of SMGO (Fig. S1b). The thickness of the as-prepared GO is about 0.75 nm (Fig. S2), validating that monolayer GO sheets were obtained. Due to the presence of functional groups in GO, its thickness is larger than that of the pristine graphene (i.e. 0.34 nm) [33]. All the chemical reagents used in this work were analytical reagents without further purification.

2.2. Synthesis of RGO film

In order to introduce nitrogen doping to the graphene sheet, the GO is reduced by EDA. First, the as-synthesized GO was suspended in *N,N*-dimethylformamide (DMF) to get homogeneous GO/DMF dispersion with a concentration of 3 mg mL^{-1}, and 30 mL GO/DMF was mixed with 20 mL dehydrated EDA in a glass flask with magnetic stirring. Then, the mixture was refluxed in an oil bath at 85 °C for 24 h [37]. Finally, RGO was obtained by filtrating the mixture and repeatedly washing with DI water. Further analysis has shown that nitrogen atoms have been successfully doped to the RGO sheet. Large-sized reduced GO (LRGO) and small-sized reduced GO (SRGO) were prepared by chemical reduction of LGGO and SMGO with the same method.

The hierarchical RGO films were prepared by combining the vacuum filtration and freeze-drying methods, as schematically illustrated in Fig. 1. First, RGO films were obtained by vacuum filtration of a certain amount of RGO dispersion through a cellulose filter paper. The vacuum filtration was immediately stopped when there is no RGO dispersion left on the filter paper. All RGO films were prepared under the same condition to make sure the remanent water left in the wet RGO films is the same for all of the samples. After the filtration, the wet RGO films were immediately peeled off from the filter paper and placed into the freeze dryer at −60 °C to freeze the water in the RGO films. Because of the continuous growth of ice crystal, the well-connected network structures in the RGO films were formed. Then, the network structures were kept by directly sublimating the water from the RGO films. In order to get the hierarchical RGO films, RGO dispersions with different compositions of LRGO sheets and SRGO sheets were used to synthesize RGO films, denoted as RGO-X (X represents the weight percent of SRGO sheets in the RGO films, ranging from 0 to 100). Note that LRGO and SRGO are uniformly distributed in water by stirring, and is immediately filtrated in less than one minute. In order to confirm the uniform distribution of LRGO and

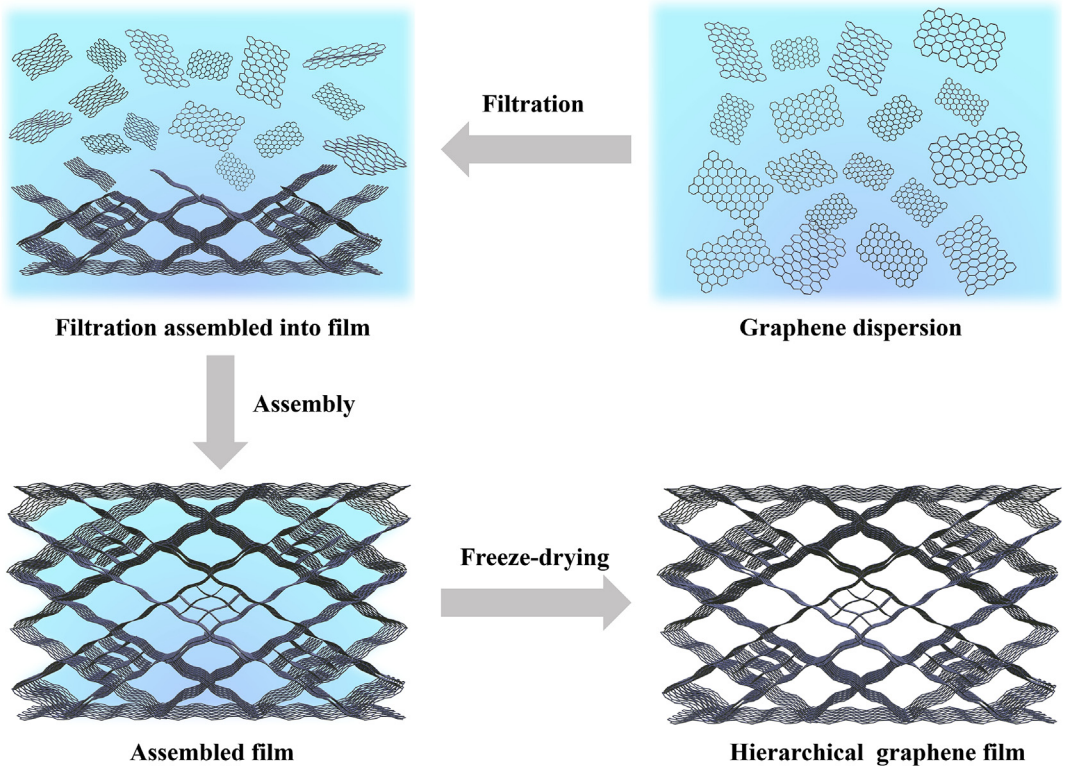

Fig. 1. Schematic illustration of the synthesis process of hierarchical RGO film.

SRGO in the RGO electrode, we have also tried the filtration with a constant stirring through a rotor (300 rpm/min) [38] and found their capacitances are similar. Thus, we think the dispersion of LRGO and SRGO is pretty good. Here, the LRGO sheets act as the backbone to form the large porous network structures and SRGO sheets act as the interlayer and interpore linkers to connect the LRGO sheets and large pores, as shown in Figs. 1 and 2(b). Therefore, it is expected that the specific surface area, electrical and ionic conductivity can be enhanced by adding proper content of SRGO sheets to LRGO sheets to form hierarchical RGO films, which is beneficial to improve their capacitive performance. By optimizing the content of SRGO sheets, the maximum capacitance of RGO electrodes is achieved.

2.3. Structural characterization

The microstructure and morphology of RGO films were characterized by field emission scanning electron microscopy (FE-SEM, Zeiss GeminiSEM 500) and transmission electron microscopy (TEM, FEI F20). Atomic force microscope (AFM) observation was carried

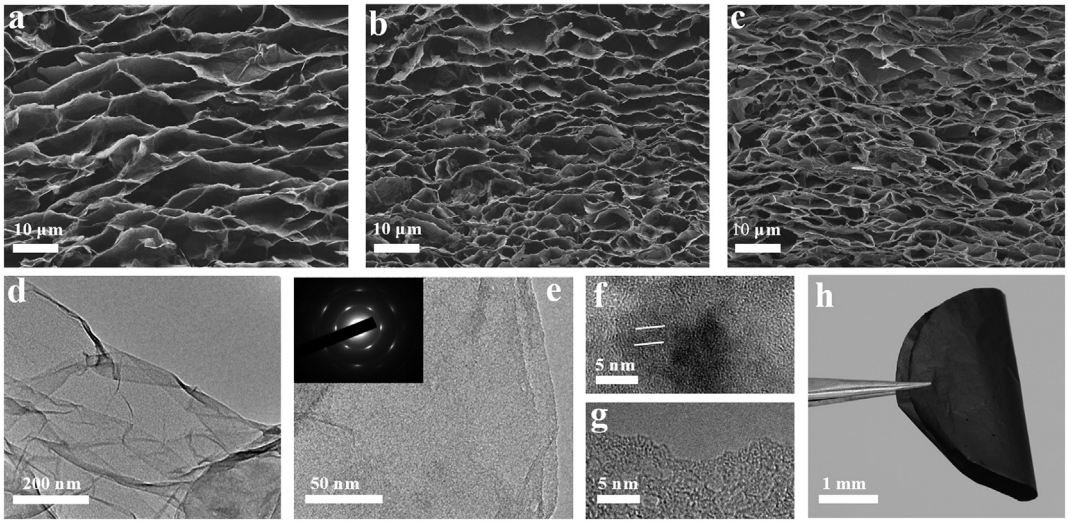

Fig. 2. SEM images of the cross section of RGO films with different content of LRGO and SRGO. (a) RGO-0, (b) RGO-40, (c) RGO-100. TEM image of RGO, (d, e) Low-magnification and (f, g) high-magnification. (h) Digital image of the flexible RGO film.

out on Oxford MFP-3D Classic to characterize the thickness of GO sheets. The electrical conductivity of RGO films was measured by the four-point probe conductivity measurement (ST2722-SD). X-ray diffraction (XRD) was performed using Bruker (Bruker D8A A25) diffractometer with Cu-Kα radiation. X-ray photoelectron spectroscopy (XPS) was conducted on the ThermoFisher K-Alpha system to investigate the chemical compositions of GO and RGO. Fourier transform infrared (FTIR) spectra were performed on Nicolet Nexus 410 with KBr pellet method. The N_2 adsorption-desorption isotherms of the RGO films were measured at 77K using ASAP 2020 instrument (Micromeritics) to characterize the pore size distribution. While, the specific surface area of the RGO films was measured by methylene blue (MB) dye adsorption method. The surface area was calculated by assuming the covering area of each absorbed microgram MB is 2.54 m^2 [39].

2.4. Electrochemical characterization

The electrochemical experiments of RGO electrode were carried out in the three-electrode system and two-electrode symmetric cell. In the three-electrode system, the RGO films were placed between two nickel foams to serve as the working electrode and the mass loading of the active materials in the working electrode was about 0.25 mg cm^{-2}. Note that although the dry RGO films exhibit good flexibility, they become brittle and loose after being placed in electrolyte for a long time as the electrolyte ions may insert into the graphene layers to make the RGO films swell. Therefore, the RGO electrode were placed between two nickel foams. One of our ongoing work is to prepare high performance flexible supercapacitor. Platinum plate, Hg/HgO electrode and 6 M KOH were served as the counter electrode, reference electrode and electrolyte, respectively. For the two-electrode symmetric setup, the electrodes were assembled in CR2032 cell with aqueous (6 M KOH) and organic electrolyte (2.0 M 1-ethyl-3-methylimidazolium ($EMIMBF_4$) in acetonitrile (AN)). Cyclic voltammetry (CV), galvanostatic charge/discharge (GCD) and electrochemical impedance spectroscopy (EIS) tests were performed using electrochemical workstation (RST 5200F) at room temperature. EIS tests were performed in the frequency range of 10 mHz–100 kHz with an AC amplitude of 5 mV.

For the three-electrode system, the specific capacitance of electrodes (C_s, F g^{-1}) were calculated from the charge/discharge plots as [7].

$$C_s = I \times \Delta t / \Delta V \times m \quad (1)$$

where I is the constant discharge current, Δt is the discharge time, ΔV is the discharge voltage, and m is the mass of the RGO films.

For the two-electrode symmetric cell, the specific capacitance C_s was calculated as [40].

$$C_s = 2 \times I \times \Delta t / \Delta V \times m \quad (2)$$

where m is the mass loading of the active material in one electrode. Energy density E (Wh kg^{-1}) of the cell was calculated as

$$E = C_s \times \Delta V^2 \Big/ 2 \times 4 \times 3.6 \quad (3)$$

And the average power density P (W kg^{-1}) of the cell was derived as

$$P = E \times 3600 / \Delta t \quad (4)$$

3. Results and discussions

3.1. Structural characteristics

Indeed, the microstructures of RGO films play an important role in determining their capacitive performance. Therefore, SEM observations were carried out to characterize the cross section of the RGO films consisted of only LRGO, 40 wt% SRGO and only SRGO sheets, as shown in Fig. 2(a)–(c), respectively. All RGO films exhibit honeycomb-like structures with well-connected networks, indicating that the pores formed by the continuous growth of ice crystals were kept during freeze-drying process. The pore size of the RGO film with only LRGO sheets (RGO-0) is about several tens of micrometer, while that of the RGO film with only SRGO sheets (RGO-100) is about several micrometer, as shown in Fig. 2(a) and (c). In contrast, the RGO films consisted of LRGO and SRGO sheets (e.g. RGO-40) exhibit hierarchical porous structures due to the interpore connection of SRGO sheets in the large pores. Besides, it will be shown that the specific surface area, electrical and ionic conductivity of the optimized RGO films are larger than those of the RGO films with pure LRGO or SRGO sheets. The intercalated SRGO between LRGO sheets is beneficial to enhance the connection of LRGO sheets and specific surface area of RGO films. TEM images of RGO sheets (Fig. 2(d) and (e)) indicate that there are many crumples. Here, the formation of mesopores is attributed to the wrinkled of graphene sheets [41] and gap between adjacent graphene sheets. The typical sixfold symmetry diffraction pattern reveals good crystallinity of RGO. The high-resolution TEM images shown in Fig. 2(f) and (g) exhibit clear lattice fringes and disorder regions. The lattices and the diffraction pattern provide further evidences for nearly complete reduction of GO. Besides, the RGO films obtained in this work have good flexibility, which promises their applications in flexible electronics, as shown in Fig. 2(h).

FTIR spectra ranging from 4000 to 600 cm^{-1} (Fig. 3(a) and Fig. S3) were carried out to characterize the chemical bonding states of the RGO and GO samples. Typically, the peaks at about 3400 cm^{-1} and 1390 cm^{-1} are ascribed to the vibration of −OH stretching [42]. While, the peaks located at 1630 cm^{-1} and 1050 cm^{-1} correspond to the stretching of −C═O and −C−O bond, respectively. Furthermore, the C−N bond stretching is observed at 1342 cm^{-1} in the RGO samples [43], revealing the successful incorporation of nitrogen atoms into the RGO sheets. Previous studies have shown that RGO can be prepared by EDA chemical reduction of GO in DMF dispersions [37].

To confirm the deoxygenation and nitrogen doping in RGO sheets by EDA reduction, XPS is carried out to characterize the chemical compositions of RGO and GO sheets. In the XPS survey scan spectra under binding energy from 0 to 1200 eV, the O1s peak for RGO sheets is significantly decreased compared to that of the GO sheets, which indicates successful reduction of GO, as shown in Fig. S4(a) and (b). Further element analysis in Fig. 3(b) shows that all of the RGO films reduced by EDA exhibit three peaks, i.e. C1s, N1s and O1s, while only C1s and O1s are observed in GO samples. The XPS results demonstrate nitrogen atoms have been successfully introduced in RGO sheets. As shown in the high resolution C1 XPS spectra of GO and RGO sheets (Fig. S4(c) and (d)), the intensities of C−O and C═O in RGO sheets are much smaller than those in GO sheets, suggesting the successful deoxygenation in the reduction process. The appearance of C−N spectra (285.7 eV) indicates the incorporation of nitrogen atoms in RGO sheets. The deconvolutions of C1s spectra for all RGO films (Fig. 3(c) and Fig. S5) are well fitted by C−C (at~284.8 eV), C−N (at~285.7 eV), C−O (at~286.8 eV), C═O (at~287.8 eV), and O═C−C (at~288.7eV) spectra [43]. Fig. 3(d) presents the high resolution N1 XPS spectra for the optimized RGO film (RGO-40), which shows that N1s spectra is comprised of four

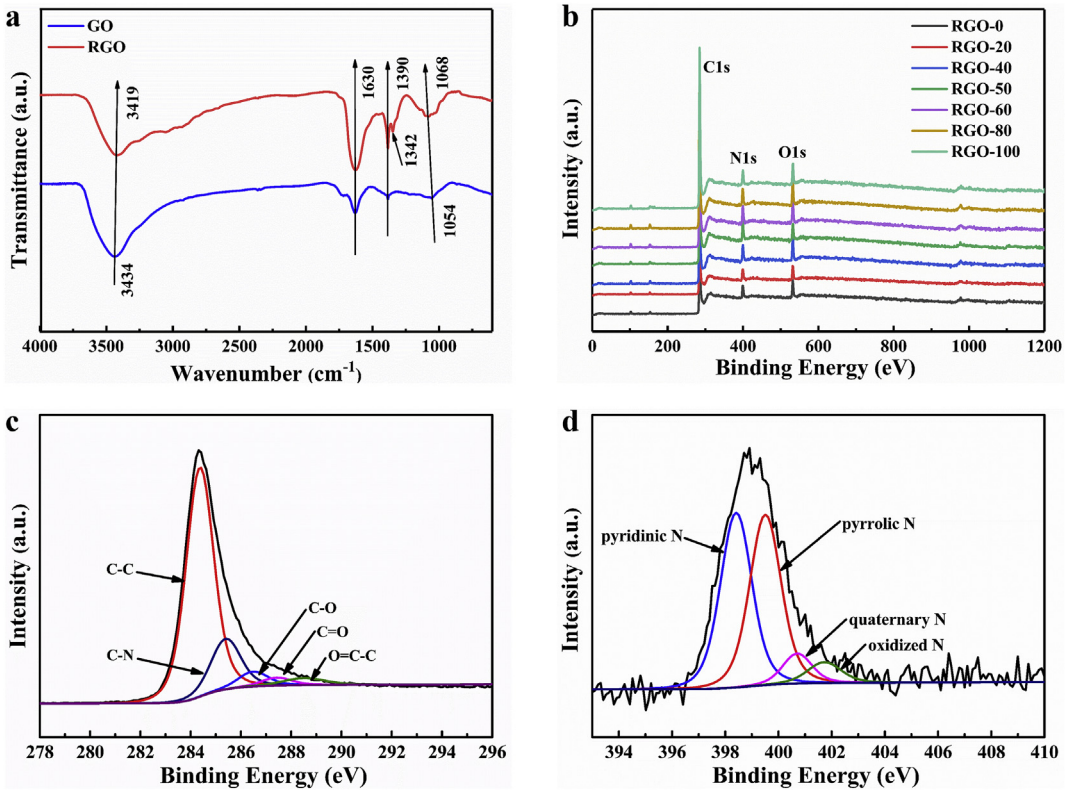

Fig. 3. (a) FTIR spectrum of LRGO and LGGO sheets. (b) XPS spectra for all RGO films with different content of LRGO and SRGO, (c) C 1s and (d) N 1s XPS spectra of the optimized RGO film.

components, revealing that there are four bonding states for nitrogen atoms in RGO sheets. The four bonding states are respectively assigned to pyridinic N (N-6 at~398.7eV), pyrrolic N (N-5 at~399.9eV), quaternary N (N-Q at~401.0eV) and oxidized N (N-X at~402.3eV) [18,44]. N-5 and N-6 are the predominant bonding states (Fig. S6). Indeed, both of the N-doping content and type have the same importance on the capacitance. Owing to the excellent electron donor characteristics and enhanced carbon catalytic activity in electron-transfer reactions, the N-5 possesses higher charge mobility and leads to the significant improvement of capacitance [45]. The N-6 can generate great pseudocapacitance and enhance the electrical conductivity, leading to enhanced capacitive performance [46]. N-6 and N-Q bond with two and three sp^2 C atoms, respectively, can donate one pair of electrons to the conductivity of π-system, which results in the enhancement of the conductivity of RGO films [47,48]. Besides, the distributed N atoms can provide the RGO films with both active sites and good wettability [47]. Moreover, N-Q groups can improve its interaction with the anions in the electrolyte and promote the formation of electric double layer, resulting in enhanced capacitance [49,50]. Therefore, the introduction of N atoms can have positive effect on the electrochemical performance. A quantitative analysis of the chemical elements for all of the RGO films is summarized in Table S1. It is shown that the RGO films with different content of LRGO and SRGO have the similar chemical compositions, and the N-6 and N-5 doping type are the predominant bonding states. Besides, further XRD measurements of the RGO and graphite sheets were conducted to show good crystallization (Fig. S7). The GO sheets exhibit a typical diffraction peak (001) at around 11.6° due to the oxygen-containing functional groups. While, the XRD patterns of RGO sheets present a board "graphene" peak, which further confirms the reduction of GO sheets [33].

The electrical conductivity of the RGO films with different content of LRGO and SRGO is measured at the room temperature, as shown in Fig. 4(a). It is shown that the electrical conductivity first increases and then decreases as the increasing of SRGO content, and the maximum electrical conductivity of 710 S m^{-1} is obtained at SRGO content 40 wt%, which is 26.2% enhancement compared to the RGO film made of pure LRGO sheets. MB dye adsorption method is used to investigate the specific surface area of RGO films, as shown in Fig. 4(a). The specific surface area has the similar trend with that of the electrical conductivity, and the maximum specific surface area of 445 m^2 g^{-1} is also reached at SRGO content 40 wt%, which is 36.1% enhancement compared to the RGO film made of pure LRGO sheets. This is because proper fraction SRGO sheets can serve as the interlayer and interpore linkers to connect LRGO sheets and large pores, which on the one hand improves the connection quality of LRGO sheets to enhance the electrical conductivity of RGO films, and on the other hand generates hierarchical porous structures to enhance the specific surface area. While, large fraction of SRGO sheets disrupt the network structures of LRGO sheets so as to decrease the electrical conductivity and specific surface area of RGO films. The specific surface area and electrical conductivity of RGO films can be quantitatively adjusted by changing the content of LRGO and SRGO sheets. Here, the specific surface area is improved by the formation of fine hierarchal structures and the electrical conductivity is improved by the well-connection of the network structures. Nitrogen adsorption-desorption isotherm is performed to further investigated the pore size distribution for the optimized RGO film (RGO-40), as Fig. S8 shown. The test shows that the RGO-40 film exhibits a Brunauer-Emmett-Teller specific surface area of about 89 m^2 g^{-1}. The pore size distribution calculated based on the nonlocal density functional theory (NLDFT) model is given in Fig. 4(b), which shows hierarchical porous structures of the RGO-40

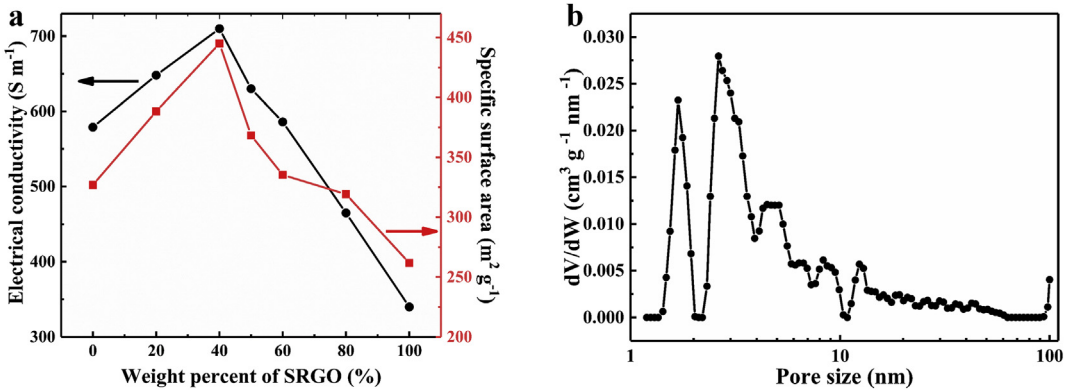

Fig. 4. (a) The specific surface area and electrical conductivity of the RGO films with different content of LRGO and SRGO. (b) The pore size distribution of RGO-40 film.

film. Note that the specific surface area of graphene films is usually smaller than that of three dimensional graphene materials, but the specific surface area is not the only factor to determine the capacitance [51,52]. The optimized RGO-40 film exhibits larger specific surface area than the previous holey graphene film, thus has larger capacitance [53,54].

3.2. Electrochemical performance

The RGO films are expected to be the promising electrode materials of supercapacitor due to their unique advantages, such as high specific surface, well-connected network structures and nitrogen doping. Here, we adopt CV, GCD and EIS tests to investigate the electrochemical performance of RGO films with different content of LRGO and SRGO sheets. The CV curves of the optimized RGO film (RGO-40) at various scan rates from 10 to 90 mV s^{-1} in the voltage window of −1.0 to 0 V are displayed in Fig. 5(a), which exhibit quasi-rectangular shapes with small humps. Here, the deviation from standard rectangular shape is attributed to the faraday pseudo-capacitance caused by the nitrogen doping and residual oxygen functional groups in the RGO sheets [55]. In addition, the CV curve of RGO-40 film at high scan rate, e.g. 500 mV s^{-1}, still maintains a similar rectangular shape, revealing excellent rate performance (Fig. S9). Like RGO-40 film, the CV curves of other RGO films also exhibit quasi-rectangular shapes at scan rate from 10 to 500 mV s^{-1} (Figs. S10 and S11). The GCD plots of the RGO-40 electrode at various current densities from 1 to 30 A g^{-1} are shown in Fig. 5(b), based on which the specific capacitance is evaluated. The curves also slightly distort from the triangular shape for ideal EDLC due to the heteroatom caused pseudocapacitance [56]. But, the triangle-like GCD curves further prove the reversible capacitive behavior of RGO films.

Fig. 5(c) presents the CV curves of the RGO films with different content of LRGO and SRGO sheets at scan rate 50 mV s^{-1}, which clearly demonstrates that the RGO-40 film has the largest enclosed area corresponding to the largest capacitance. Fig. 5(d) shows the relation between the specific capacitance and SRGO content at the current density 1 A g^{-1}. The specific capacitance first increases and then decreases as the increasing of SRGO content. The maximum specific capacitance 429.7 F g^{-1} is obtained at SRGO content 40 wt%, which is 61.9% enhancement compared to that of RGO film with pure LRGO sheets. The relation of the specific capacitance to SRGO content agrees well with that of the electric conductivity and specific surface area, see Figs. 4(a) and 5(d). Besides, chemical element analysis shown in Table. S1 has proved the similar nitrogen doping type of the RGO films with different content of SRGO. Therefore, compared to RGO-0 electrode, the enhanced capacitance of RGO-40 electrode primarily comes from the enhanced specific surface area (i.e. 36.1% enhancement in specific surface area due to the formation of fine hierarchical structures) and the well-connection of the network structures (i.e. 26.2% enhancement in electrical conductivity). While, RGO-100 electrode has the smallest electrical conductivity (340 S m^{-1}) and specific surface area (261 m^2 g^{-1}), leading to the smallest specific capacitance. In this work, we can precisely control the specific surface area and electrical conductivity of RGO electrode by simply adjusting the content of LRGO and SRGO sheets in the RGO films, which provides a robust routine to tune the capacitance of RGO electrodes.

Fig. 5(e) describes the relations between the specific capacitance and current density for all RGO films based on GCD tests. Typically, the specific capacitance decreases as the increasing of current density. Among the RGO films, RGO-40 electrode is superior to other RGO electrodes in term of the rate performance, and the capacitance decreases from 429.7 F g^{-1} to 339.9 F g^{-1} as the current density increases from 1 A g^{-1} to 30 A g^{-1}. The 79.1% capacitance retention demonstrates the good rate performance of RGO-40 electrode due to the fast ion transfer (hierarchical porous structures) and electron transfer (well-connected network structures). Indeed, the hierarchical porous structures can supply ion-buffering reservoirs and ion-transport pathway to enhance the ionic conductivity of the RGO electrodes as will be shown in the following content. For comparison, the specific capacitance of the graphene-based materials published in the previous literatures is summarized in Table S2. The optimized RGO film developed in this work has a relatively large specific capacitance. In practical applications of supercapacitors, cycle stability is another crucial factor to evaluate the performance of the electrode materials. Electrochemical stability of RGO-40 electrode is performed under a constant charge/discharge current density of 5A g^{-1} for 10,000 cycles at room temperature. RGO-40 electrode exhibits excellent cycle stability with the capacitance retention of 91.16% (Fig. 5(f)).

The EIS spectrum is an important indicator to evaluate the ion transfer resistance of the RGO films. Fig. 6(a) presents the EIS curves for all of the RGO electrodes and the magnification at the high frequency region is shown in Fig. 6(b), which exhibit straight lines at low frequency region and deformed semicircles at high frequency region. In order to further understand the electrochemical behaviors of all electrode, the EIS data is fitted to an equivalent circuit model shown in the inset of Fig. 6(a) by adopting Z-view software, where R_s represents the intrinsic ohmic resistance calculated by the intercept between the Nyquist plot and Z′ axis, R_{ct} represents interfacial charge transfer resistance derived as the difference between the end point of the semicircle region of Nyquist plot and R_s in Z′ axis, R_{Wo} represents the Warburg diffusion

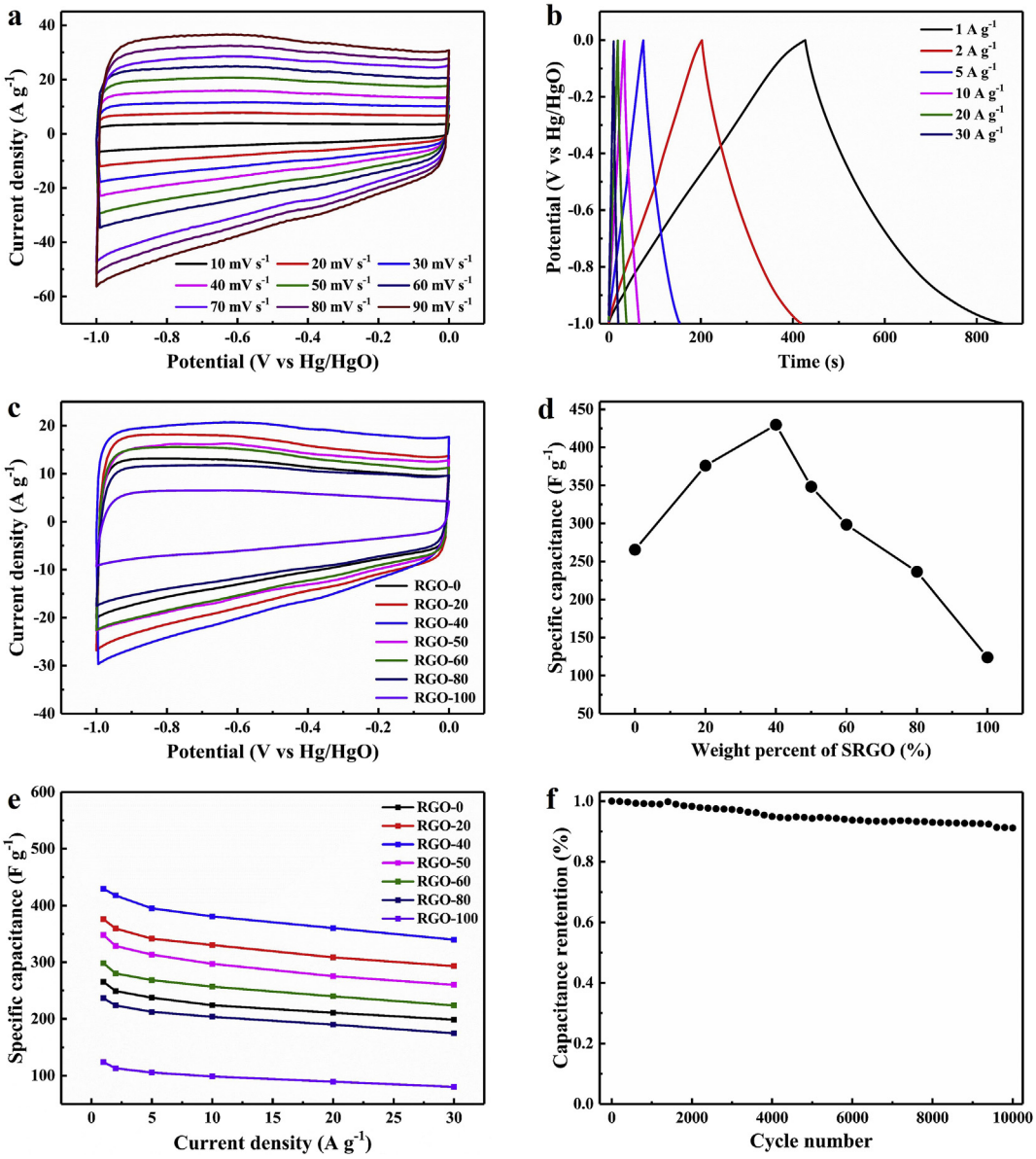

Fig. 5. (a) CV curves of the RGO-40 film under different scan rates. (b) GCD curves of the RGO-40 films under different current densities. (c) CV curves of RGO films with different content of LRGO and SRGO sheets at scan rate 50 mV s^{-1}. (d) The specific capacitance of RGO films at 1 A g^{-1}. (e) The specific capacitance of RGO films at different densities. (f) The cycle performance of RGO-40 film at 5 A g^{-1}.

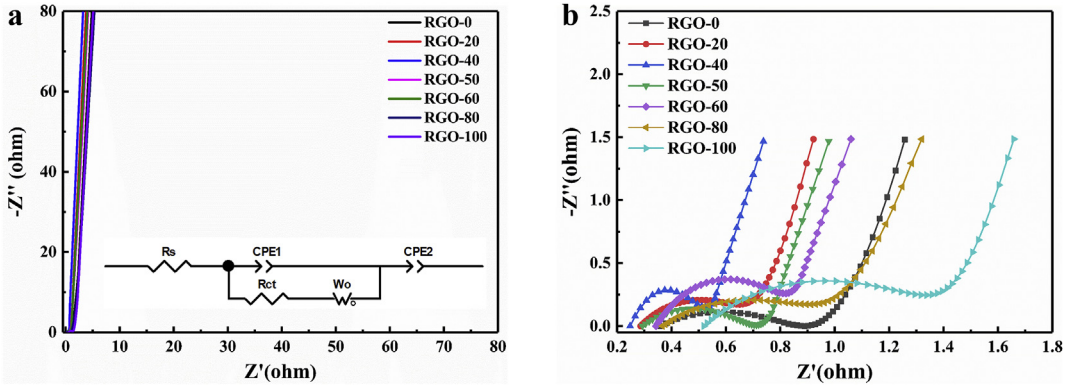

Fig. 6. (a) EIS plots of RGO electrodes and the diagram of the equivalent circuit (inset). (b) The magnification of the high-frequency region.

resistance determined by the difference between the start point of the straight line at low frequency region and the end point of the semicircle region at high frequency region in Z′ axis, see Fig. S12(a) [40]. R_{ct} mainly comes from the electronic and ionic resistance at the interface between the electrode and electrolyte, which is mainly determined by the wettability between the electrolyte and electrode, the morphology and conductivity of electrode. R_{Wo} comes from the resistance of ion diffusion from electrolyte into the electrode. The optimized RGO-40 electrode has the smallest R_s (0.248 Ω), R_{ct} (0.292 Ω) and R_{Wo} (0.04 Ω) values, representing 31%, 44.8% and 70.1% reduction, respectively, compared to the RGO electrode made of pure LRGO sheets, see Fig. S12(b). This reveals that the RGO-40 electrode exhibits the highest ability of the charge transfer and ion migration in the porous structures. The hierarchical and well-connected network structures of the RGO-40 film are beneficial for the electrolyte ion transfer, which is favorable for the excellent rate performance of the RGO-40 electrode.

In order to confirm the energy and power density of the RGO-40 electrode, the CV and GCD tests were carried out in a two-electrode symmetrical cell with 6 M KOH aqueous electrolyte. Fig. 7(a) depicts the CV plots of the RGO-40 symmetric cell at different scan rates from 10 to 90 mV s^{-1}. The CV curves of the two-electrode system also show almost rectangular and symmetric shapes. More CV plots at larger scan rates from 100 to 500 mV s^{-1} are shown in Fig. S13 and the similar rectangular shapes are observed. The GCD plots at various current densities are presented in Fig. 7(b). All curves exhibit fast current-voltage response and symmetric triangular shape, which reveals high columbic efficiency of the RGO-40 based symmetric supercapacitor [16].

Fig. 7(c) displays the specific capacitance of the RGO-40 based symmetric supercapacitor obtained by the GCD curves at various current densities. The specific capacitance of the symmetric cell at

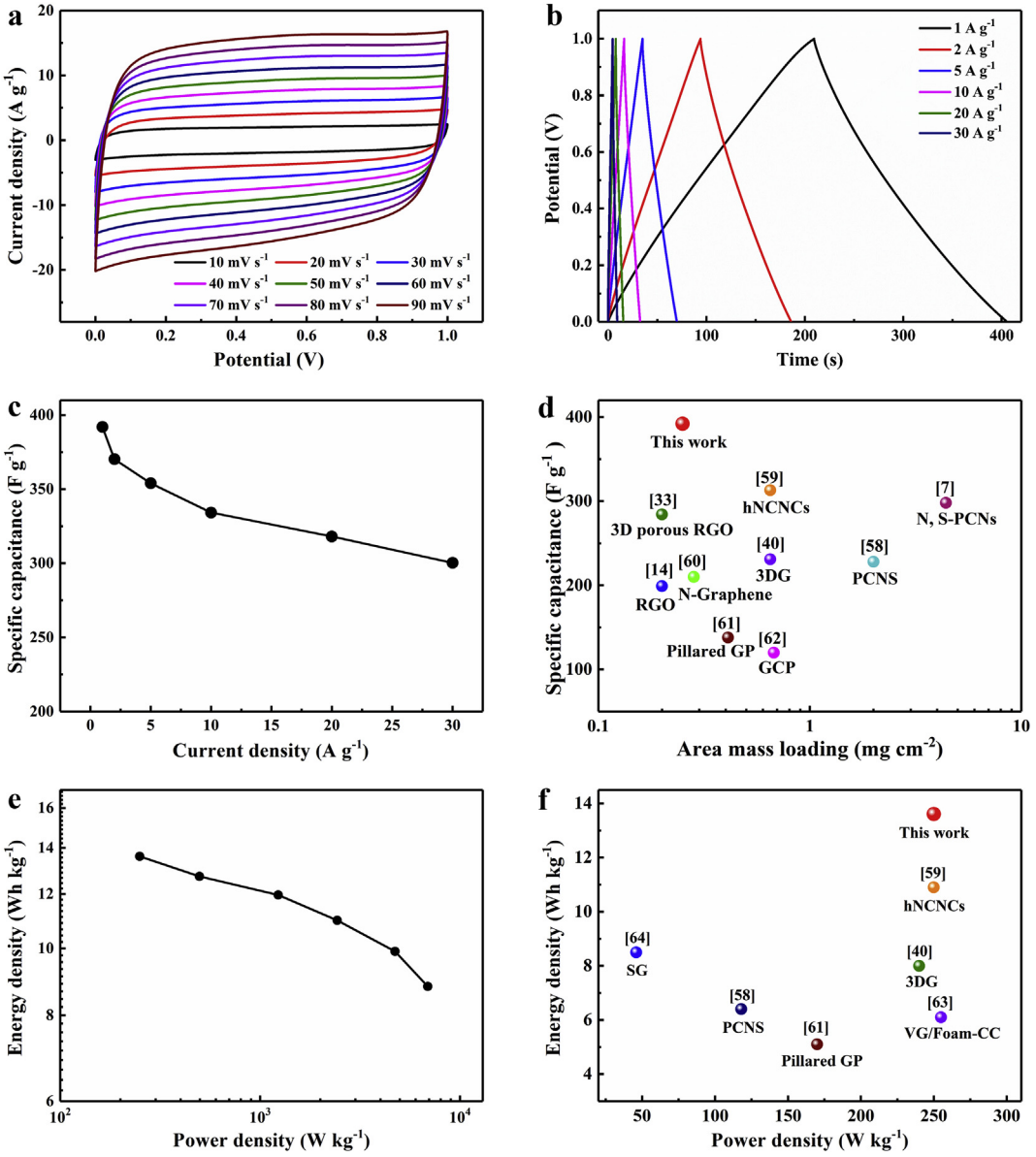

Fig. 7. Capacitive performance of the RGO-40 based symmetric cell in aqueous electrolyte. (a) CV plots at various scan rates. (b) GCD curves at different current densities. (c) Specific capacitance versus current density. (d) Comparison of the specific capacitance of the RGO-40 based symmetric supercapacitor and other carbon based symmetric supercapacitors in aqueous electrolyte [7,14,33,40,58–62]. (e) Ragone plots of the energy density versus power density of supercapacitor. (f) Energy density versus power density for the RGO-40 based symmetric supercapacitor and other carbon based symmetric supercapacitors in aqueous electrolyte [40,58,59,61,63,64].

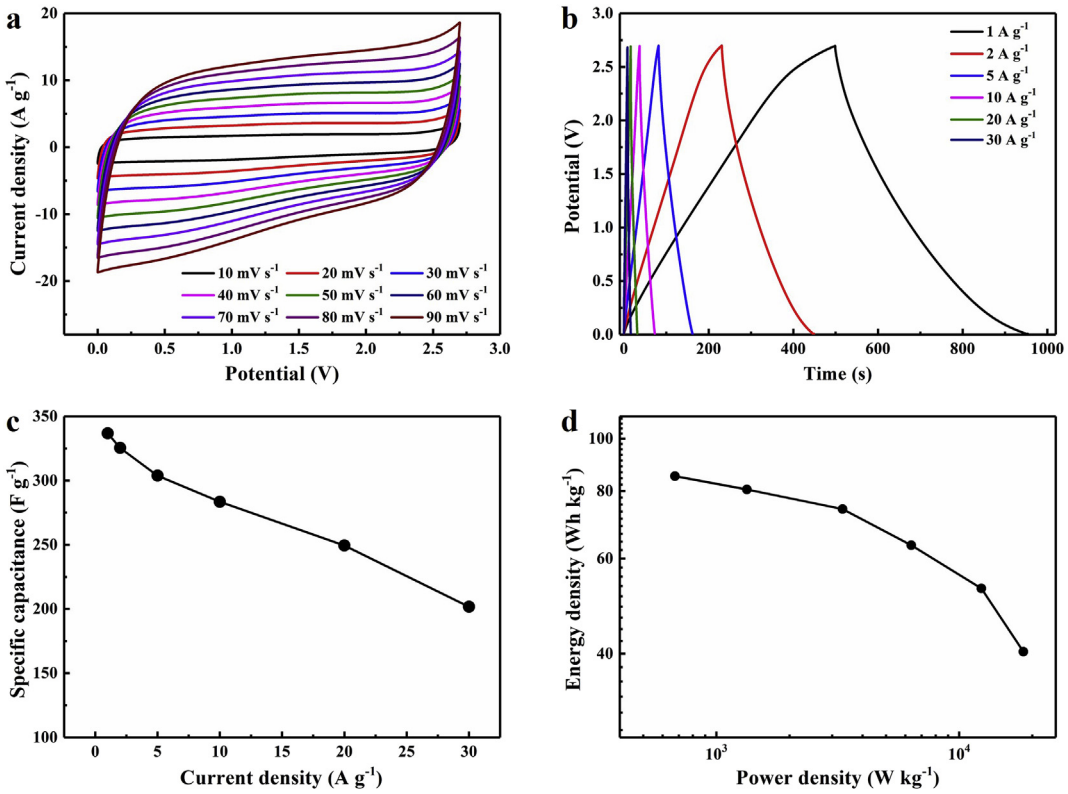

Fig. 8. Capacitive performance of the RGO-40 based symmetric cell in organic electrolyte. (a) CV plots at various scan rates. (b) GCD curves at different current densities. (c) Specific capacitance versus current density. (d) Ragone plots of the energy density versus power density of supercapacitor.

1A g^{-1} is about 391.9 F g^{-1}, which is lower than the value obtained in the three-electrode system (429.7 F g^{-1}) as in KOH electrolyte one of the electrode works in the voltage window of −0.5-0 V which usually exhibits smaller capacitance [57]. Indeed, the mass loading is an important factor and the specific capacitance of film-like electrode usually decreases as the increasing of the film thickness due to the increased resistance of electron and ion. The RGO-40 electrode presented in this work has the moderate loading mass, but the highest specific capacitance among the previously reported carbon based electrodes, as shown in Fig. 7(d). Indeed, we didn't find the decay of the specific capacitance as the increasing of RGO-40 electrode thickness due to its well-connected hierarchical network structures. However, for thick RGO-40 film it becomes brittle and is hard to fabricate the RGO-40 electrode without damage. Therefore, one of our ongoing work is to increase the flexibility of the RGO films with hierarchical network structures to improve the loading mass of the RGO electrodes.

According to the above GCD tests, the energy and power density of the RGO-40 based symmetric supercapacitor are calculated based on Eqs. (2)–(4). The Ragone plot of the RGO-40 based symmetric supercapacitor in aqueous electrolyte is shown in Fig. 7(e). In general, the energy density of the supercapacitor decreases as the increasing of power density due to the electrical and ionic resistance. However, for the optimized RGO-40 films, the well-connected network and hierarchical porous structures lead to very small electrical and ionic resistance, so that its energy density is 13.61 Wh kg^{-1} for power density of 250 W kg^{-1} and the energy density is still 10.99 Wh kg^{-1} for the power density increasing to 2.43 kW kg^{-1}. The comparison of the energy density and power density for the RGO-40 based symmetric supercapacitor and other carbon based symmetric supercapacitor in aqueous electrolytes are presented in Fig. 7(f). The results further demonstrate the good capacitive performance of RGO films based supercapacitors by properly adjusting their microstructures and heteroatom doping.

In order to achieve higher energy density, RGO-40 based supercapacitors in organic electrolyte were further tested to evaluate their electrochemical performance. The operating voltage of the supercapacitor with organic electrolyte can be extended to 2.7 V, as shown in Fig. 8(a) and (b). The RGO-40 electrodes deliver a high specific capacitance of 336.7 F g^{-1} in EMIMBF$_4$/AN electrolyte at current density of 1A g^{-1} (see Fig. 8(c)) due to the well-connected network and hierarchical porous structures of RGO-40 electrode. The specific capacitance retains 59.9% when the current density increases 30A g^{-1}, which is smaller than that in aqueous electrolyte because of the relatively lower ion-diffusion in organic electrolyte. Owing to a higher operating voltage, RGO-40 based supercapacitors in organic electrolyte deliver an energy density of 85.2 Wh kg^{-1} at a power density of 675 W kg^{-1} as shown in Fig. 8(d). Furthermore, the supercapacitors can achieve an energy density of 63.5 Wh kg^{-1} at a power density of 6.35 kW kg^{-1}. Indeed, we have also reviewed the capacitance of graphene related electrodes in organic electrolyte and the comparison of the capacitance is shown in Table S3 and the capacitance of RGO-40 electrode is closed to the largest value of the holey graphene related electrode in organic electrolyte.

4. Conclusions

In conclusion, we have fabricated the nitrogen doped RGO films with well-connected hierarchal structures by combining the vacuum filtration and freeze-drying methods. The specific surface area and electrical conductivity of RGO films can be precisely controlled by adjusting the content of LRGO and SRGO sheets in the RGO films, where LRGO sheets act the backbone to form the network structures and the SRGO sheets act as the interlayer and interpore

connectors to connect the LRGO sheets and large pores. A maximum specific capacitance of 429.7 F g^{-1} at current density 1A g^{-1} is achieved for the optimized RGO film at SRGO content of 40 wt %, which is 61.9% improvement compared to the RGO films with pure LRGO sheets. Meanwhile, the specific surface area and electrical conductivity of the optimized RGO film also reach the maximum values that are 36.1% and 26.2% improvement compared to RGO film of pure LRGO. Therefore, the improved capacitance primarily comes from the increasing of specific surface area due to the formation of fine hierarchical structures and the better connection of the network structures (the increasing of electrical conductivity) for the optimized RGO electrode. Besides, the optimized RGO-40 electrode shows excellent cycle, rate performance, power and energy density. The facile strategy for synthesizing the RGO films with hierarchical structures presented herein could provide more opportunities for a variety of energy storage applications of graphene related materials, including supercapacitors and Li-ion batteries.

Acknowledgments

The authors acknowledge the financial support from the National Key Research and Development Program of China (No. 2016YFB0700300) and National Natural Science Foundation of China (No. 11572239).

Appendix A. Supplementary data

Supplementary data to this article can be found online at https://doi.org/10.1016/j.electacta.2018.12.071.

References

[1] P. Simon, Y. Gogotsi, Materials for electrochemical capacitors, Nat. Mater. 7 (2008) 845–854.
[2] M. Ghidiu, M.R. Lukatskaya, M.Q. Zhao, Y. Gogotsi, M.W. Barsoum, Conductive two-dimensional titanium carbide 'clay' with high volumetric capacitance, Nature 516 (2014) 78–81.
[3] H. Jeon, J.M. Jeong, S.B. Hong, M.H. Yang, J. Park, D.H. Kim, S.Y. Hwang, B.G. Choi, Facile and fast microwave-assisted fabrication of activated and porous carbon cloth composites with graphene and MnO_2 for flexible asymmetric supercapacitors, Electrochim. Acta 280 (2018) 9–16.
[4] H. Ji, X. Zhao, Z. Qiao, J. Jung, Y. Zhu, Y. Lu, L.L. Zhang, A.H. MacDonald, R.S. Ruoff, Capacitance of carbon-based electrical double-layer capacitors, Nat. Commun. 5 (2014) 3317.
[5] V. Augustyn, P. Simon, B. Dunn, Pseudocapacitive oxide materials for high-rate electrochemical energy storage, Energy Environ. Sci. 7 (2014) 1597–1614.
[6] Y.Z. Chao, S.B. Chen, H.Q. Chen, X.J. Hu, Y. Ma, W.S. Gao, Y.X. Bai, Densely packed porous graphene film for high volumetric performance supercapacitor, Electrochim. Acta 276 (2018) 118–124.
[7] Y.J. Li, G.L. Wang, T. Wei, Z.J. Fan, P. Yan, Nitrogen and sulfur co-doped porous carbon nanosheets derived from willow catkin for supercapacitors, Nanomater. Energy 19 (2016) 165–175.
[8] Z.S. Wu, A. Winter, L. Chen, Y. Sun, A. Turchanin, X. Feng, K. Mullen, Three-dimensional nitrogen and boron co-doped graphene for high-performance all-solid-state supercapacitors, Adv. Mater. 24 (2012) 5130–5135.
[9] D. Li, M.B. Muller, S. Gilje, R.B. Kaner, G.G. Wallace, Processable aqueous dispersions of graphene nanosheets, Nat. Nanotechnol. 3 (2008) 101–105.
[10] S. Stankovich, D.A. Dikin, R.D. Piner, K.A. Kohlhaas, A. Kleinhammes, Y. Jia, Y. Wu, S.T. Nguyen, R.S. Ruoff, Synthesis of graphene-based nanosheets via chemical reduction of exfoliated graphite oxide, Carbon 45 (2007) 1558–1565.
[11] H. Li, Y. Tao, X.Y. Zheng, J.Y. Luo, F.Y. Kang, H.M. Cheng, Q.H. Yang, Ultra-thick graphene bulk supercapacitor electrodes for compact energy storage, Energy Environ. Sci. 9 (2016) 3135–3142.
[12] I.L. Tsai, J.Y. Cao, L.L. Fevre, B. Wang, R. Todd, R.A.W. Dryfe, A.J. Forsyth, Graphene-enhanced electrodes for scalable supercapacitors, Electrochim. Acta 257 (2017) 372–379.
[13] M.D. Stoller, S. Park, Y. Zhu, J. An, R.S. Ruoff, Graphene-based ultracapacitors, Nano Lett. 8 (2008) 3498–3502.
[14] Y. Chen, X.O. Zhang, D.C. Zhang, P. Yu, Y.W. Ma, High performance supercapacitors based on reduced graphene oxide in aqueous and ionic liquid electrolytes, Carbon 49 (2011) 573–580.
[15] J.H. Lee, N. Park, B.G. Kim, D.S. Jung, K. Im, J. Hur, J.W. Choi, Restacking-inhibited 3D reduced graphene oxide for high performance supercapacitor electrodes, ACS Nano 7 (2013) 9366–9374.
[16] P. Hao, Z.H. Zhao, Y.H. Leng, J. Tian, Y.H. Sang, R.I. Boughton, C.P. Wong, H. Liu, B. Yang, Graphene-based nitrogen self-doped hierarchical porous carbon aerogels derived from chitosan for high performance supercapacitors, Nanomater. Energy 15 (2015) 9–23.
[17] X.W. Dong, N.T. Hu, L.M. Wei, Y.J. Su, H. Wei, L. Yao, X.L. Li, Y.F. Zhang, A new strategy to prepare N-doped holey graphene for high-volumetric supercapacitors, J. Mater. Chem. A 4 (2016) 9739–9743.
[18] M. Yu, J.D. Zhang, S.M. Li, Y.B. Meng, J.H. Liu, Three-dimensional nitrogen doped holey reduced graphene oxide framework as metal-free counter electrodes for high performance dye-sensitized solar cells, J. Power Sources 308 (2016) 44–51.
[19] Z. Liu, L.L. Jiang, L.Z. Sheng, Q.H. Zhou, T. Wei, B.S. Zhang, Z.J. Fan, Oxygen clusters distributed in graphene with "paddy land" structure: ultrahigh capacitance and rate performance for supercapacitors, Adv. Funct. Mater. 28 (2018) 1705258.
[20] B. Li, F. Dai, Q.F. Xiao, L. Yang, J.M. Shen, C.M. Zhang, M. Cai, Nitrogen-doped activated carbon for a high energy hybrid supercapacitor, Energy Environ. Sci. 9 (2016) 102–106.
[21] B. Papandrea, X. Xu, Y.X. Xu, C.Y. Chen, Z.Y. Lin, G.M. Wang, Y.Z. Luo, M. Liu, Y. Huang, L.Q. Mai, X. Duan, Three-dimensional graphene framework with ultra-high sulfur content for a robust lithium–sulfur battery, Nano Res. 9 (2016) 240–248.
[22] S.Y. Gan, L.J. Zhong, T.S. Wu, D.X. Han, J.D. Zhang, J. Ulstrup, Q.J. Chi, L. Niu, Spontaneous and fast growth of large-area graphene nanofilms facilitated by oil/water interfaces, Adv. Mater. 24 (2012) 3958–3964.
[23] S. Gilje, S. Han, M. Wang, K.L. Wang, R.B. Kaner, A chemical route to graphene for device applications, Nano Lett. 7 (2007) 3394–3398.
[24] Y.L. Shao, H.Z. Wang, Q.H. Zhang, Y.G. Li, Fabrication of large-area and high-crystallinity photoreduced graphene oxide films via reconstructed two-dimensional multilayer structures, NPG Asia Mater. 6 (2014) e119.
[25] F. Gunes, H.J. Shin, C. Biswas, G.H. Han, E.S. Kim, S.J. Chae, J.Y. Choi, Y.H. Lee, Layer-by-layer doping of few-layer graphene film, ACS Nano 4 (2010) 4595–4600.
[26] Y.G. Niu, J.P. Zhao, X. Zhang, X.J. Wang, J. Wu, Y. Li, Y. Li, Large area orientation films based on graphene oxide self-assembly and low temperature thermal reduction, Appl. Phys. Lett. 101 (2012) 181903.
[27] H. Chen, M.B. Muller, K.J. Gilmore, G.G. Wallace, D. Li, Mechanically strong, electrically conductive, and biocompatible graphene paper, Adv. Mater. 20 (2008) 3557–3561.
[28] X. Yang, L. Qiu, C. Cheng, Y. Wu, Z.F. Ma, D. Li, Ordered gelation of chemically converted graphene for next-generation electroconductive hydrogel films, Angew. Chem. Int. Ed. 50 (2011) 7325–7328.
[29] X.W. Yang, C. Cheng, Y.F. Wang, L. Qiu, D. Li, Liquid-mediated dense integration of graphene materials for compact capacitive energy storage, Science 341 (2013) 534–537.
[30] Z.Y. Xiong, C.L. Liao, W.H. Han, X.G. Wang, Mechanically tough large-area hierarchical porous graphene films for high-performance flexible supercapacitor applications, Adv. Mater. 27 (2015) 4469–4475.
[31] X.W. Yun, Z.Y. Xiong, L. Tu, L.Q. Bai, X.G. Wang, Hierarchical porous graphene film: an ideal material for laser-carving fabrication of flexible micro-supercapacitors with high specific capacitance, Carbon 125 (2017) 308–317.
[32] Z.Y. Xiong, X.W. Yun, B. Tang, X.G. Wang, Ultratough cellular films from graphene oxide hydrogel: a way to exploit rigidity and flexibility of two-dimensional honeycomb carbon, Carbon 107 (2016) 548–556.
[33] Y. Shao, M.F. El-Kady, C.W. Lin, G. Zhu, K.L. Marsh, J.Y. Hwang, Q. Zhang, Y. Li, H. Wang, R.B. Kaner, 3D freeze-casting of cellular graphene films for ultrahigh-power-density supercapacitors, Adv. Mater. 28 (2016) 6719–6726.
[34] G. Xin, T. Yao, H. Sun, S.M. Scott, D. Shao, G. Wang, J. Lian, Highly thermally conductive and mechanically strong graphene fibers, Science 349 (2015) 1083–1087.
[35] H.T. Sun, L. Mei, J.F. Liang, Z.P. Zhao, C. Lee, H.L. Fei, M.N. Ding, J.T. Lau, M.F. Li, C. Wang, X. Xu, G.L. Hao, B. Papandrea, I. Shakir, B. Dunn, Y. Huang, X.F. Duan, Three-dimensional holey-graphene/niobia composite architectures for ultrahigh-rate energy storage, Science 356 (2017) 599–604.
[36] W.S.H. Jr, R.E. Offeman, Preparation of graphitic oxid, J. Am. Chem. Soc. 80 (1958) 1339.
[37] J.F. Che, L.Y. Shen, Y.H. Xiao, A new approach to fabricate graphene nanosheets in organic medium: combination of reduction and dispersion, J. Mater. Chem. 20 (2010) 1722–1727.
[38] J. Chen, Y.R. Li, L. Huang, N. Jia, C. Li, G.Q. Shi, Size fractionation of graphene oxide sheets via filtration through track-etched membranes, Adv. Mater. 27 (2015) 3654–3660.
[39] M.J. McAllister, J.L. Li, D.H. Adamson, H.C. Schniepp, A.A. Abdala, J. Liu, M. Herrera-Alonso, D.L. Milius, R. Car, R.K. Prud'homme, I.A. Aksay, Single sheet functionalized graphene by oxidation and thermal expansion of graphite, Chem. Mater. 19 (2007) 4396–4404.
[40] J. Zhao, Y.F. Jiang, H. Fan, M. Liu, O. Zhuo, X.X. Wang, Q. Wu, L.J. Yang, Y.W. Ma, Z. Hu, Porous 3D few-layer graphene-like carbon for ultrahigh-power supercapacitors with well-defined structure-performance relationship, Adv. Mater. 29 (2017) 1604569.
[41] T.T. Yang, R.Y. Li, X.H. Long, Z.J. Li, Z.G. Gu, G.L. Wang, J.K. Liu, Nitrogen and sulphur-functionalized multiple graphene aerogel for supercapacitors with excellent electrochemical performance, Electrochim. Acta 187 (2016) 143–152.

[42] N.H. Kim, T. Kuila, J.H. Lee, Simultaneous reduction, functionalization and stitching of graphene oxide with ethylenediamine for composites application, J. Mater. Chem. A 1 (2013) 1349–1358.
[43] L. Hu, P.P. Jiang, P.B. Zhang, G. Bian, S.S. Sheng, M. Huang, Y.M. Bao, J.L. Xia, Amine-graphene oxide/waterborne polyurethane nanocomposites: effects of different amine modifiers on physical properties, J. Mater. Sci. 51 (2016) 8296–8309.
[44] S.C. Hou, X. Cai, H.W. Wu, X. Yu, M. Peng, K. Yan, D.C. Zou, Nitrogen-doped graphene for dye-sensitized solar cells and the role of nitrogen states in triiodide reduction, Energy Environ. Sci. 6 (2013) 3356–3362.
[45] Y.J. Li, K. Ye, K. Cheng, D.X. Cao, Y. Pan, S.Y. Kong, X.M. Zhang, G.L. Wang, Anchoring CuO nanoparticles on nitrogen-doped reduced graphene oxide nanosheets as electrode material for supercapacitors, J. Electroanal. Chem. 727 (2014) 154–162.
[46] K.L. Wang, M. Xu, Y. Gu, Z.R. Gu, J. Liu, Q.H. Fan, Low-temperature plasma exfoliated n-doped graphene for symmetrical electrode supercapacitors, Nanomater. Energy 31 (2017) 486–494.
[47] W.L. Zhang, C. Xu, C.Q. Ma, G.X. Li, Y.Z. Wang, K.Y. Zhang, F. Li, C. Liu, H.M. Cheng, Y.W. Du, N.J. Tang, W.C. Ren, Nitrogen-superdoped 3D graphene networks for high-performance supercapacitors, Adv. Mater. 29 (2017) 1701677.
[48] Y. Liu, Y.T. Shen, L.T. Sun, J.C. Li, C. Liu, W.C. Ren, F. Li, L.B. Gao, J. Chen, F.C. Liu, Y.Y. Sun, N.J. Tang, H.M. Cheng, Y.W. Du, Elemental superdoping of graphene and carbon nanotubes, Nat. Commun. 7 (2016) 10921.
[49] Y.F. Deng, Y. Xie, K.X. Zou, X.L. Ji, Review on recent advances in nitrogen-doped carbons: preparations and applications in supercapacitors, J. Mater. Chem. A 4 (2016) 1144–1173.
[50] O. Ornelas, J.M. Sieben, R. Ruiz-Rosas, E. Morallon, D. Cazorla-Amoros, J. Geng, N. Soin, E. Siores, B.F. Johnson, On the origin of the high capacitance of nitrogen-containing carbon nanotubes in acidic and alkaline electrolytes, Chem. Commun. 50 (2014) 11343–11346.
[51] B. Zhao, P. Liu, Y. Jiang, D.Y. Pan, H.H. Tao, J.S. Song, T. Fang, W.W. Xu, Supercapacitor performances of thermally reduced graphene oxide, J. Power Sources 198 (2012) 423–427.
[52] L.H. Lu, W.F. Li, L.S. Zhou, Y.J. Zhang, Z. Zhang, Y. Chen, J.H. Liu, L.W. Liu, W. Chen, Y.G. Zhang, Impact of size on energy storage performance of graphene based supercapacitor electrode, Electrochim. Acta 219 (2016) 463–469.
[53] Q.Q. Zhou, M. Zhang, J. Chen, J.D. Hong, G.Q. Shi, Nitrogen-doped holey graphene film-based ultrafast electrochemical capacitors, ACS Appl. Mater. Interfaces 8 (2016) 20741–20747.
[54] Y.X. Xu, C.Y. Chen, Z.P. Zhao, Z.Y. Lin, C. Lee, X. Xu, C. Wang, Y. Huang, M.L. Shakir, X.F. Duan, Solution processable holey graphene oxide and its derived macrostructures for high-performance supercapacitors, Nano Lett. 15 (2015) 4605–4610.
[55] X.J. Wei, X.Q. Jiang, J.S. Wei, S.Y. Gao, Functional groups and pore size distribution do matter to hierarchically porous carbons as high-rate-performance supercapacitors, Chem. Mater. 28 (2016) 445–458.
[56] Q. Liang, L. Ye, Z.H. Huang, Q. Xu, Y. Bai, F. Kang, Q.H. Yang, A honeycomb-like porous carbon derived from pomelo peel for use in high-performance supercapacitors, Nanoscale 6 (2014) 13831–13837.
[57] Z. Li, L. Zhang, B.S. Amirkhiz, X.H. Tan, Z.W. Xu, H.L. Wang, B.C. Olsen, C.M.B. Holt, D. Mitlin, Carbonized chicken eggshell membranes with 3D architectures as high-performance electrode materials for supercapacitors, Adv. Energy Mater. 2 (2012) 431–437.
[58] X.M. Fan, C. Yu, J. Yang, Z. Ling, C. Hu, M.D. Zhang, J.S. Qiu, A layered-nano-space-confinement strategy for the synthesis of two-dimensional porous carbon nanosheets for high-rate performance supercapacitors, Adv. Energy Mater. 5 (2015) 1401761.
[59] J. Zhao, H.W. Lai, Z.Y. Lyu, Y.F. Jiang, K. Xie, X.Z. Wang, Q. Wu, L.J. Yang, Z. Jin, Y.W. Ma, J. Liu, Z. Hu, Hydrophilic hierarchical nitrogen-doped carbon nanocages for ultrahigh supercapacitive performance, Adv. Mater. 27 (2015) 3541–3545.
[60] E. Haque, M.M. Islam, E. Pourazadi, M. Hassan, S.N. Faisal, A.K. Roy, K. Konstantinov, A.T. Harris, A.I. Minett, V.G. Gomes, Nitrogen doped graphene via thermal treatment of composite solid precursors as a high performance supercapacitor, RSC Adv. 5 (2015) 30679–30686.
[61] G.K. Wang, X. Sun, F.Y. Lu, H. Sun, M.P. Yu, W.L. Jiang, C.S. Liu, J. Lian, Flexible pillared graphene-paper electrodes for high-performance electrochemical supercapacitors, Small 8 (2012) 452–459.
[62] Z. Weng, Y. Su, D.W. Wang, F. Li, J.H. Du, H.M. Cheng, Graphene-cellulose paper flexible supercapacitors, Adv. Energy Mater. 1 (2011) 917–922.
[63] Z. Bo, W.G. Zhu, W. Ma, Z.H. Wen, X.R. Shuai, J.H. Chen, J.H. Yan, Z.H. Wang, K.F. Cen, X.L. Feng, Vertically oriented graphene bridging active-layer/current-collector interface for ultrahigh rate supercapacitors, Adv. Mater. 25 (2013) 5799–5806.
[64] X.B. Wang, Y.J. Zhang, C.Y. Zhi, X. Wang, D.M. Tang, Y.B. Xu, Q.H. Weng, X.F. Jiang, M. Mitome, D. Golberg, Y. Bando, Three-dimensional strutted graphene grown by substrate-free sugar blowing for high-power-density supercapacitors, Nat. Commun. 4 (2013) 2905.